ARTICLES
PUBLISHED ONLINE: 17 MARCH 2013 | DOI: 10.1038/NPHOTON.2013.42
nature photonics

Weyl points and line nodes in gyroid photonic crystals

Ling Lu*, Liang Fu, John D. Joannopoulos and Marin Soljačić

Weyl points and line nodes are three-dimensional linear point and line degeneracies between two bands. In contrast to two-dimensional Dirac points, which are their lower-dimensional analogues, Weyl points are stable in momentum space, and the associated surface states are predicted to be topologically non-trivial. However, Weyl points are yet to be discovered in nature. Here, we report photonic crystals based on double-gyroid structures, exhibiting frequency-isolated Weyl points with complete phase diagrams by breaking the parity and time-reversal symmetries. Gapless surface dispersions associated with non-zero Chern numbers are demonstrated. Line nodes are also found in similar geometries, the associated surface states forming flat dispersion bands. Our results are based on realistic *ab initio* calculations with true predictive power and should be readily realizable experimentally from microwave to optical frequencies.

Two-dimensional (2D) Dirac points are unique linear-dispersion point degeneracies in 2D periodic systems. For example, most of the remarkable properties of graphene are tied to the Dirac points at its Fermi level[1,2]. In photonics, 2D Dirac cones significantly alter the dynamics of photons[3,4] and thus enable novel applications[5–7]. Topologically[8], opening up the 2D Dirac point degeneracies can generate topologically non-trivial frequency gaps inside which unidirectional 1D edge states are protected against disorder[9–12]. Similarly, it is expected that if a material could be found that exhibits three-dimensional (3D) linear dispersion relations between frequency (energy) and wave vector ($\mathbf{k}$), it would also display a wide range of interesting phenomena. Such 3D linear point degeneracies between two bands are called 'Weyl points'. Recently, a few proposals[13–16] have been made as to how the rich physics of Weyl points[17–20] could be demonstrated in electronics. However, no observation of Weyl points has yet been reported.

In this Article, we perform analytical and numerical studies to predict a new realization of Weyl points using 3D photonic crystals. A key advantage of this photonic system, in contrast to the proposed electronic systems, is the ease of its eventual experimental realization and the associated characterization of the Weyl points. Specifically, we demonstrate frequency-isolated Weyl points in a perturbed double-gyroid (DG) photonic crystal system. We present complete phase diagrams, topologically protected surface states, as well as frequency-isolated linear line degeneracies ('line nodes') and their flat-band surface states.

Before proceeding, we first point out one intriguing distinction between the 2D Dirac points and the 3D Weyl points. 2D Dirac cones are not robust; they are only protected by the product of time-reversal symmetry (T) and parity (P) inversion. In two dimensions, the Dirac cone effective Hamiltonian takes the form of $H(\mathbf{k}) = v_x k_x \sigma_x + v_z k_z \sigma_z$, where v_i are the group velocities and σ_i are the Pauli matrices. This form is protected by PT (product of P and T), which requires $H(\mathbf{k})$ to be real. Thus, one can open a gap in this dispersion relation upon introducing a perturbation, proportional to

$$\sigma_y = \begin{pmatrix} 0 & -i \\ i & 0 \end{pmatrix},$$

that is imaginary; for example, even an infinitesimal perturbation that breaks just P or just T will open a gap. In contrast, 3D Weyl points are topologically protected gapless dispersions robust against any perturbation. In three dimensions, Weyl point dispersions are governed by the Weyl Hamiltonian $H(\mathbf{k}) = v_x k_x \sigma_x + v_y k_y \sigma_y + v_z k_z \sigma_z$. The σ_y term can exist only when PT is broken; indeed, this is a necessary condition for the existence of Weyl points. Because all three Pauli matrices are used in the Hamiltonian, there is no possibility of constructing a term that can open a gap in this two-band degeneracy of 3D periodic systems, thereby making a single Weyl point absolutely robust to perturbations. The only way to eliminate and create Weyl points is through pair-annihilations and pair-generations of Weyl points of opposite chiralities, which typically requires a strong perturbation. The chirality ($c = \pm 1$) of a Weyl point can be defined as $c = \mathrm{sgn}(\det[v_{ij}])$ for $H(\mathbf{k}) = k_i v_{ij} \sigma_j$. It can also be defined by the Chern number of a closed surface enclosing the single Weyl point in momentum space.

The organization of this Article is as follows. Our starting point for obtaining Weyl points and line nodes is a DG photonic crystal with a band structure that exhibits a threefold degeneracy (quadratic in all three directions) at the Brillouin zone centre (Γ) in an otherwise complete bandgap. We first obtain the line nodes by applying a perturbation preserving P and T and show the controlled flat band surface states in the surface Brillouin zone. Second, we obtain the Weyl points by applying perturbations breaking either P or T and explore the phase diagrams when both P and T are broken. Third, we present the Chern numbers of the Weyl points and the topologically non-trivial surface states associated with them. Finally, we discuss various opportunities for experimental realizations.

Gyroid photonic crystals

The gyroid, discovered by Schoen[21] in 1970, is an infinitely connected bi-continuous triply periodic minimal surface containing no straight lines. Consisting of triple junctions in a body-centred cubic (bcc) lattice, the gyroid surface can be approximated by isosurfaces of $g(\mathbf{r}) = \sin(2\pi x/a)\cos(2\pi y/a) + \sin(2\pi y/a)\cos(2\pi z/a) + \sin(2\pi z/a)\cos(2\pi x/a)$ (ref. 22), where a is the lattice constant. The space group of a single gyroid (SG) is $I4_132$ (no. 214)[23–25], which lacks inversion; adding its inversion counterpart $g(-\mathbf{r})$ gives the DG structure belonging to $Ia\bar{3}d$ (no. 230), which is a

Department of Physics, Massachusetts Institute of Technology, Cambridge, Massachusetts 02139, USA. *e-mail: linglu@mit.edu

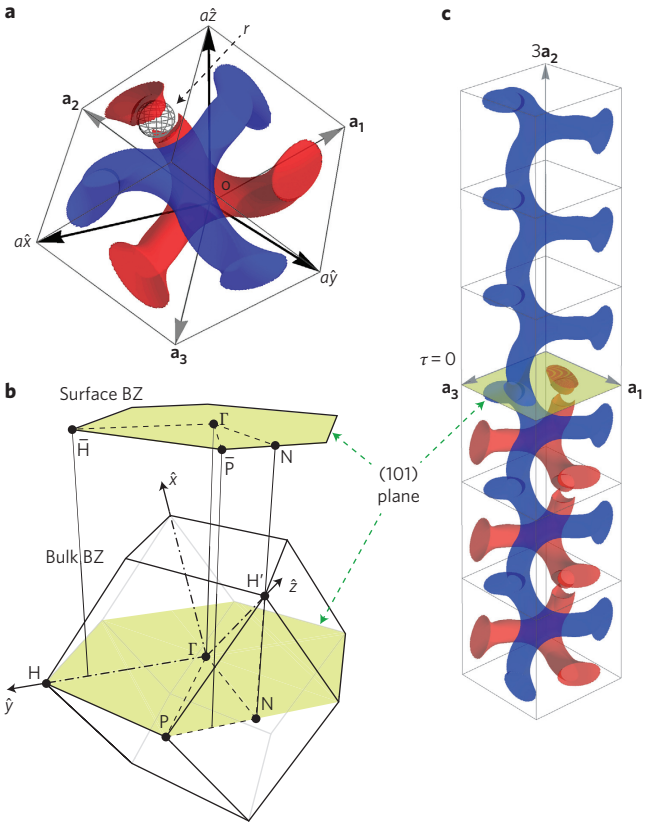

Figure 1 | Real-space unit cell and reciprocal-space Brillouin zone of the gyroid photonic crystals. a, Real-space geometry in a bcc unit cell where $\mathbf{a}_1 = (-1, 1, 1)a/2$, $\mathbf{a}_2 = (1, -1, 1)a/2$ and $\mathbf{a}_3 = (1, 1, -1)a/2$. The two identical gyroid structures in red and blue are high-refractive-index ($n = 4$) materials; they are inversion pairs with respect to the origin (o). The illustrated air-sphere of radius r ($r/a = 0.13$) located at $(1/4, -1/8, 1/2)a$ is only placed there when structural symmetry needs to be broken. **b**, The bulk and (101) surface Brillouin zones of the bcc lattice. Weyl points and line nodes investigated in this work lie in the green (101) plane through the origin (Γ) of the bulk Brillouin zone, projecting onto the (101) surface Brillouin zone. Γ-N is along $[\bar{1}01]$ and Γ-H is along [010] ($\hat{y}$). **c**, An air-isolated DG surface can be formed by terminating the perturbed gyroid (red) but not the other (blue). The SG photonic crystal on top has a large complete bandgap, as shown in Fig. 2a.

direct-product group of $I4_132$ and inversion. The red gyroid in Fig. 1a is defined by filling the inner space of the isosurface ($g(\mathbf{r}) > 1.1$) with high-refractive-index material ($\sqrt{\varepsilon} = n = 4$) and air otherwise. The magnetic permeability μ is unity everywhere. (These values for the dielectrics correspond to germanium and air at optical frequencies.) The blue gyroid is the inversion counterpart of the red gyroid with respect to the origin; the two gyroids do not overlap in space. The band structures of both the SG photonic crystal and the DG photonic crystal are plotted in Fig. 2a in orange and blue, respectively. The SG photonic crystal[26] has a 32% complete bandgap between the second and third bands from 0.42 to 0.58 in normalized frequencies. The DG photonic crystal band structure[26] contains a unique frequency-isolated threefold degeneracy among the third, fourth and fifth bands at the centre of the Brillouin zone (Γ), which is highlighted by green ellipses in Fig. 2a. The first and second bands are almost degenerate, as are the third and fourth bands, which concave downwards and touch the fifth band, which concaves upwards. The threefold degenerate point is well isolated in frequency from other states in the band structure, making it an ideal starting point for applying symmetry-breaking perturbations.

Line nodes and their flat surface bands

The threefold degeneracy of quadratic dispersions at Γ can be lifted by breaking the $I4_132$ space group without breaking P or T symmetries. This is done by replacing a part of the gyroid material with two air-spheres (one on each gyroid). The first air-sphere is placed in the red gyroid as illustrated in Fig. 1a, and the other is its inversion counterpart in the blue gyroid (not shown in Fig. 1a). This perturbation lifts the fifth band out of the threefold degeneracy with the third and fourth bands at Γ, as shown in Fig. 2b. The fourth and fifth bands cross one another linearly, forming a closed line degeneracy around the Γ point in the (101) plane through Γ, inside an otherwise complete frequency gap. The area enclosed by this nodal line can be controlled by the strength of the perturbations (the radii of the air-spheres).

Similar to the line-node semimetals[27], the surface states associated with this line-node bulk bandstructure contain flat dispersion bands. We constructed an interface between the DG and SG photonic crystals by removing only the perturbed gyroid (Fig. 1c). The suface states are trapped by the pseudo-gap of the DG and the full gap of the SG. We define a termination parameter τ ($0 \leq \tau < 1$) to indicate the periodically equivalent termination positions along the [101] direction. $\tau = 0$ is set at the origin of the unit cell, as shown in Fig. 1c.

Figure 3a shows one surface band in the bulk pseudo-gap of the original DG photonic crystal of quadratic point degeneracy. When τ increases periodically, the surface dispersion, at every surface $\mathbf{k}$ point, moves from the air band (conduction band) through the pseudo-gap to the dielectric band (valence band)[28]. At Γ, the surface dispersion is pinned into the bulk states at the degeneracy point. The surface band of $\tau = 0.0$, except for the $\bar{\text{H}}$–$\bar{\text{P}}$ region, is very flat. The high density of states associated with the flat surface dispersion is potentially useful for enhancing the light–matter interactions at the surface. Even more interesting surface states are shown in Fig. 3b for the line-node photonic crystal. The nodal line bulk states project onto the (101) surface Brillouin zone as a closed line that separates the surface Brillouin zone into two disconnected areas. So, the surface dispersions can be flat bands in either of the two regions in the Brillouin zone. The green dispersion in Fig. 3b has all its frequencies nearly degenerate inside the line-node area, while the red dispersion is relatively flat in the rest of the Brillouin zone. The general features of the flat surface dispersions do not change when the line-node photonic crystal is terminated by other means. For example, when the SG photonic crystal is replaced by air, one could selectively enhance, by changing the surface terminations, the light emission of surface sources into either radiative or non-radiative surface modes (that is, inside or outside the light cone of air).

Phase diagrams of Weyl points under PT-breaking

In what follows, we break the PT symmetry to obtain Weyl points of photons for the first time. We start by individually breaking P or T of the DG photonic crystal, and then consider the general case where P and T are broken simultaneously.

First, we break P while preserving T. Because T maps a Weyl point at $\mathbf{k}$ to $-\mathbf{k}$ with the same chirality (as velocities and σ_y change signs), there must exist at least two other Weyl points, both of opposite chirality, to neutralize the whole system. So, the minimal number of Weyl points in this case has to be four. As illustrated in Fig. 1a, we break P by placing only one air-sphere on one of the gyroids (but not the other) at the middle point of two neighbouring triple junctions. Under this pure P-breaking perturbation, two pairs of Weyl points, shown in Fig. 2c, emerge along Γ-N and Γ-H directions. The fact that all the Weyl points appear along high-symmetry lines significantly simplifies the analysis. There are no other states in the vicinity of the Weyl points' frequencies.

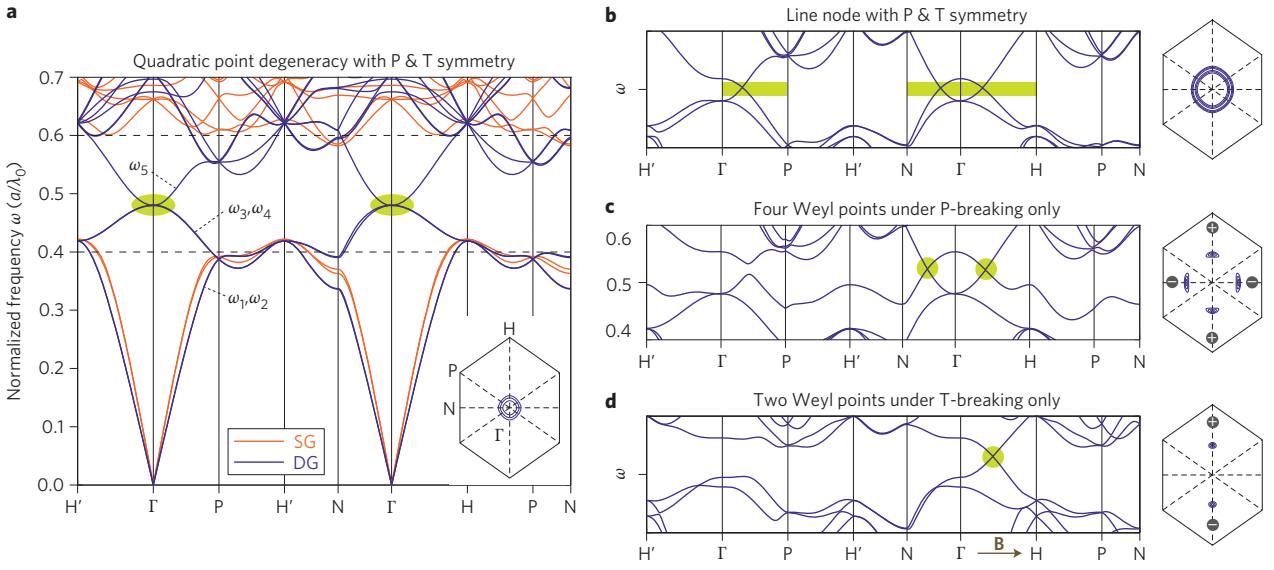

Figure 2 | Gapless photonic band structures of the DG photonic crystals. a–d, Band structures without (**a**) and with (**b–d**) perturbations. All the dispersion behaviours close to the degeneracy points in this figure can be described well by the low-energy theory model in Supplementary Section SB. Because P and T are not broken at the same time in these photonic crystals, **k** and $-\mathbf{k}$ are degenerate in the band structures. A few lowest-value contours of the frequency difference between the fourth and fifth bands are shown (hexagonal insets) for each band structure in the (101) plane. The contour spacing is 0.004 in normalized frequency, and '+' and '−' are used to label the chiralities of the Weyl points. **a**, The original DG photonic-crystal band structure has a threefold degeneracy at Γ among the third, fourth and fifth bands in a pseudo-gap. The SG photonic crystal has a huge frequency gap covering the pseudo-gap frequency region. **b**, We place the two air-spheres on the two gyroids: one air-sphere ($r/a = 0.07$) is located at $(1/4, -1/8, 1/2)a$, the other is its inversion symmetric counterpart. Under this perturbation, the fourth and fifth bands touch linearly in a closed line around Γ in the (101) plane. The linear crossing line is highlighted by a green stripe; this structure does not yet exhibit any Weyl points. **c**, We apply a P-breaking perturbation by placing one air-sphere ($r/a = 0.10$) in one of the gyroids, but not the other. Two pairs of Weyl points appear (highlighted by green circles): one pair appears along Γ-H and the other along Γ-N. **d**, We apply a T-breaking perturbation (P conserved) by applying a d.c. magnetic field (dimensionless $|\mathbf{B}| = 0.875$) to the DG photonic crystal without air-spheres. Only one pair of Weyl points appears (highlighted by the green circle), along the direction of the magnetic field (Γ-N).

We next apply d.c. magnetic fields **B** (along different directions) to the original DG photonic crystal structure of Fig. 2a to break T while preserving P. We assume the high-index gyroid material is gyroelectric and use a generic model[29] to describe its magnetic response. When **B** is along $\hat{z}$, we assume the permittivity tensor takes the form of

$$\varepsilon(|\mathbf{B}|) = \begin{pmatrix} \varepsilon_{11}(|\mathbf{B}|) & i\varepsilon_{12}(|\mathbf{B}|) & 0 \\ -i\varepsilon_{12}(|\mathbf{B}|) & \varepsilon_{11}(|\mathbf{B}|) & 0 \\ 0 & 0 & \varepsilon \end{pmatrix} \quad (1)$$

where $\det(\varepsilon(|B|)) = (\varepsilon_{11}^2(|B|) - \varepsilon_{12}^2(|B|))\varepsilon = \varepsilon^3$; this constant determinant condition ensures the dispersions as a whole do not move much in frequency with the external d.c. **B** fields. The dimensionless effective magnetic field intensity is defined as $|\mathbf{B}| \equiv \varepsilon_{12}/\varepsilon$ in this Article. When the **B** field is along other directions, the corresponding ε tensor can be obtained via coordinate transformations. (Note that T-breaking can be implemented equally well via μ for gyromagnetic materials[10]). Under this pure T-breaking perturbation, only a single pair of Weyl points emerges along the direction of the magnetic field, as shown in Fig. 2d. This is the minimum number of Weyl points that can exist with inversion symmetry. These two Weyl points are frequency-degenerate: P maps a Weyl point at **k** to $-\mathbf{k}$ with the opposite chirality (because velocities change signs).

Third, we apply both P- and T-breaking perturbations continuously, at the same time, to observe the phase transitions between the two (II) Weyl points in the pure T-breaking phase and the four (IV) Weyl points in the pure P-breaking phase. Interestingly, different magnetic field directions produce strikingly different phase diagrams. When **B** is applied along Γ-H, only two phases exist: the T-breaking dominated phase (II) and the P-breaking dominated phase (IV). The pure P-breaking phase, shown in the contour plot Fig. 2c, has four Weyl points: two with positive chiralities along Γ-H and two with negative chiralities along Γ-N. Applying a magnetic field along the Γ-H direction drives the two negative-chirality Weyl points towards the lower positive one. Increasing the magnetic field further annihilates two of the Weyl points of opposite chiralities and the system enters the T-breaking dominated phase,

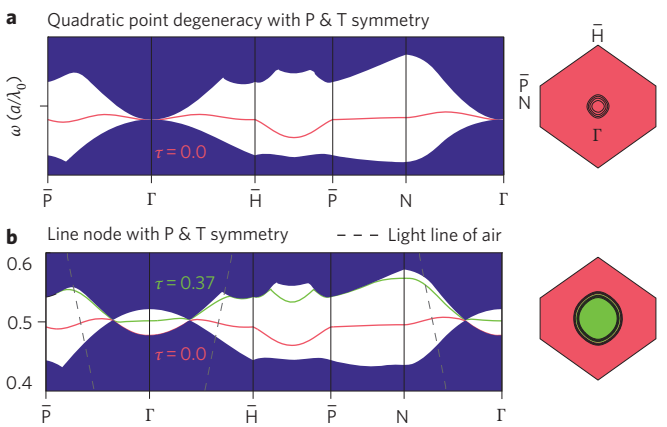

Figure 3 | Flat surface dispersions of two pseudo-gapped photonic crystals. **a**, A flat surface dispersion at the interface between the SG and the original DG of a bulk quadratic point degeneracy as in Fig. 2a. **b**, Two surface dispersions at the interfaces between the SG and the line-node DG photonic crystal in Fig. 2b. They are flat in two different regions of the surface Brillouin zone separated by the projected line-node bulk states. The two surface Brillouin zones on the right are coloured in the regions where the surface states are flat.

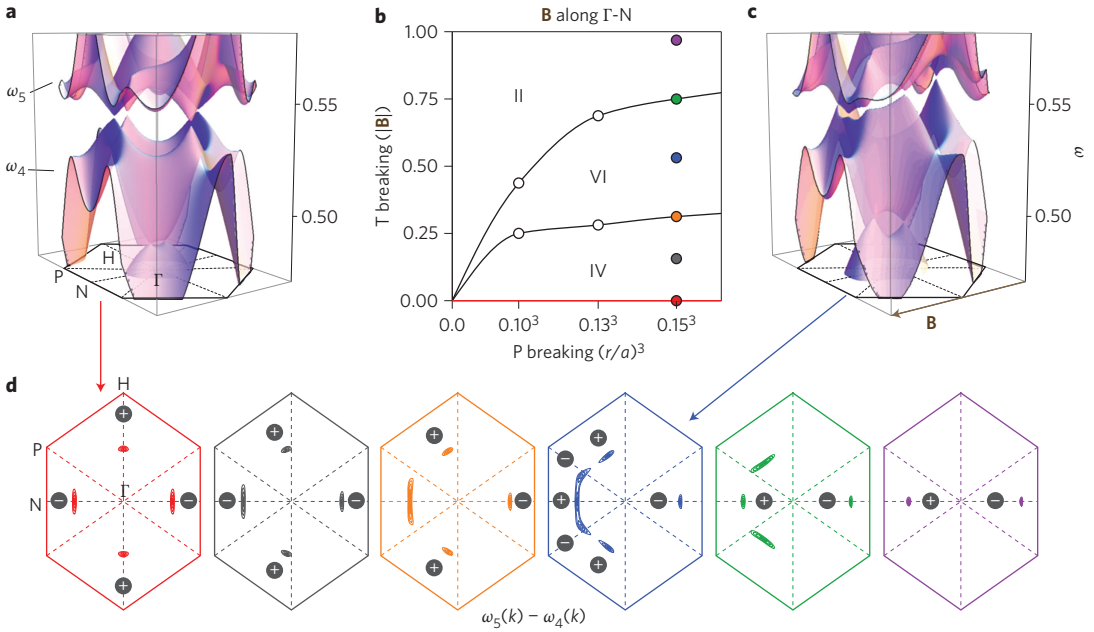

Figure 4 | Phase diagram of Weyl points when the magnetic field is applied along Γ-N. a,**c**, Two surface dispersion plots showing the entire band dispersions $\omega(\mathbf{k})$ of the third, fourth and fifth bands for two particular cases, where $\mathbf{k}$ lies in the (101) surface Brillouin zone in Fig. 1b. **b**, Each phase in this phase diagram is labelled by the number (Roman numerals) of Weyl points. The phase transition line is found by scanning the **B** field amplitude in the calculation for three different P-breaking strengths. The pure P-breaking phase (*x*-axis) is highlighted in red; it is realizable at optical frequencies in essentially lossless materials. **d**, Six 2D contour plots showing the locations of the Weyl points at representative positions in the phase diagram (the contour spacing is 0.002 in normalized frequency). The contour plots share the same colour as the circles of their corresponding positions in the phase diagram in **b**.

which has only two Weyl points along Γ-H. A detailed description of this phase diagram is shown in Supplementary Fig. SA.

An even richer phase diagram, shown in Fig. 4, appears when we switch the magnetic field to the Γ-N direction. The system undergoes two phase transitions from the P-breaking dominated phase (IV) to the T-breaking dominated phase (II). The extra intermediate phase (VI) of six Weyl points is generated when one of the negative-chirality Weyl points in the pure P-breaking phase (red contour plot) splits (orange contour plot) into three Weyl points (blue contour plot) under the increasing **B** field. Of these three Weyl points, the original Weyl point flips its chirality from negative to positive, and the other two negative Weyl points move away from their creation position towards the neighbouring two positive ones. The two pairs of Weyl points eventually meet (green contour plot) and annihilate simultaneously, leaving the remaining two Weyl points (purple contour plot) along the direction of the magnetic field (Γ-N). When two Weyl points annihilate, the band dispersions are quadratic along the directions in which they meet.

In general, P-T phase diagrams depend on the form of the perturbations: the d.c. magnetic field can be oriented along arbitrary directions and, in addition, there are many different ways to break the inversion symmetry. We also note that there are new topological phases outside of the Weyl-point phases. For example, by further increasing the T-breaking strength in phase II of Fig. 4, the two Weyl points could annihilate around the Brillouin zone boundary and enter a new topologically non-trivial phase of a complete 3D bandgap that resembles the 3D quantum Hall effect in electronics[30].

Chern numbers and non-trivial surface states

Weyl points are topologically stable objects in the 3D Brillouin zone: they act as monopoles of Berry flux in momentum space, and are therefore intimately related to the topological invariant known as the Chern number[31]. The Chern number can be defined for a single bulk band or a set of bands, where the Chern numbers of the individual bands are summed, on any closed 2D surface in the 3D Brillouin zone. The difference of the Chern numbers defined on two surfaces, of all bands below the Weyl point frequencies, equals the sum of the chiralities of the Weyl points enclosed between the two surfaces[18]. In Fig. 5a we illustrate the Chern numbers of the 2D planes perpendicular to Γ-H($\hat{y}$); these are closed surfaces in the 3D periodic Brillouin zone. The first contour plot (red), of a pure P-breaking phase in Fig. 4, is used as an example. The Chern number of all lower bands on the plane is plotted in light blue on the left side. The Chern number vanishes when the plane is outside the Weyl points. It changes by 1 when the plane moves across one Weyl point and changes by 2 when the plane crosses two Weyl points of the same chirality.

As a result of the non-zero Chern numbers of all the lower bulk bands (first, second, third and fourth), there are topologically protected gapless chiral surface states inside the bandgap (between fourth and fifth bands) away from the Weyl points. This is a higher-dimensional generalization of the protection of one-way chiral edge states (1D) by the non-zero Chern numbers of the 2D bulk bands[13,32]. An example of the non-trivial gapless surface dispersion, along a line cut in the 2D surface Brillouin zone in Fig. 5a, is plotted in Fig. 5b. A surface mode profile is also shown. Because T is not broken in this example, the surface dispersions are degenerate between $\mathbf{k}$ and $-\mathbf{k}$ while the Chern number flips sign. Similar to the 'Fermi arcs' in Weyl semimetals[13,18], at the frequency of the Weyl points, the surface dispersions connect the Weyl points (of opposite chiralities) as line segments that do not close in the surface Brillouin zone. The above analysis on Chern numbers and surface modes applies for surfaces terminated along other directions and for other Weyl-point phases as well.

Proposals for experimental realizations

The theoretical predictions discussed above can be readily realized using many available materials and fabrication techniques, and the bulk and surface dispersions can be verified by transmission experiments[33,34]. The line nodes and the Weyl-point phases of pure P-breaking perturbations, without T-breaking, can be realized

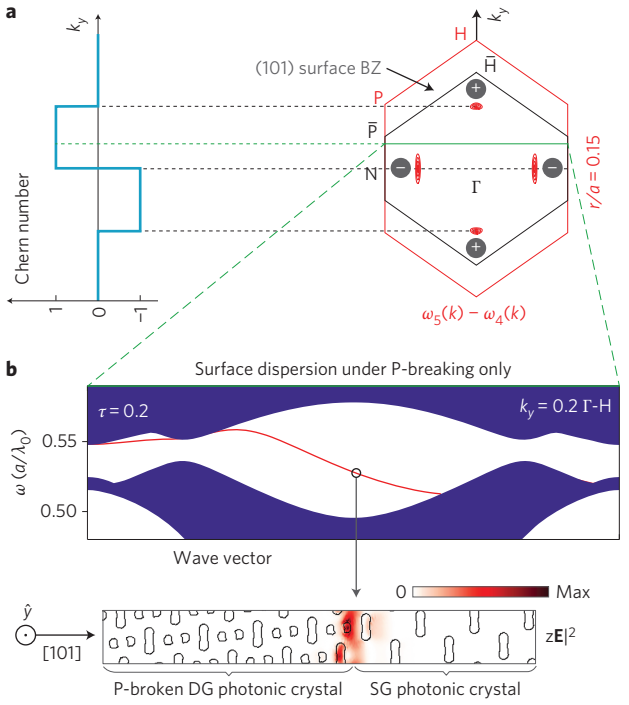

Figure 5 | Topological surface states of a Weyl-point photonic crystal. **a**, The non-zero Chern number of the plane moving along $\hat{k}_y$ in the 3D bulk Brillouin zone. The Chern number is summed over the bulk bands below the Weyl-point frequency. **b**, An example of a topologically protected surface state of a Weyl-point photonic crystal. The projected bulk states are plotted in blue in the surface bandstructure, and the gapless surface state dispersion relation is plotted in red. The spatial field distribution ($|\mathbf{E}|^2$) of one surface mode, at the centre of the **k**-axis, is plotted with the contour outlines of the refractive index profile. The surface state is localized at the interface between the DG photonic crystal and the SG photonic crystal.

from optical to microwave frequencies. The Weyl-point phases involving T-breaking can be realized with gyromagnetic materials at microwave frequencies[10].

The gyroid structures can be made by either bottom-up or top-down approaches. In nature, gyroid geometries are found in butterfly wings[35], lipid mesophases[36], liquid crystals[37] and block co-polymers[38,39]. At optical wavelengths, germanium can either be directly synthesized[40] into DG strucutures or backfilled[41] into DG templates made by self-assembly. Top-down 3D fabrications such as interference lithography[42], direct writing[43], angled-etching (for the SG)[44,45], membrane-stacking[46] and 3D printing are all good candidates for making the gyroid structures.

Conclusions

In summary, this article provides a detailed design of the minimum number of frequency-isolated Weyl points and line nodes along the high-symmetry lines and planes in the Brillouin zone of a DG photonic crystal system. Complete P–T phase diagrams are investigated by means of annihilations and creations of Weyl pairs. The topologically non-trivial surface states of Weyl-point photonic crystals and flat surface dispersions of line-node photonic crystals are presented. This work may open doors to new paradigms in photonics: topologically protected 2D chiral surface states realizable at optical frequencies, radiation-controllable photonic density of states enhanced by flat surface dispersions, possible new 3D topological phases of complete frequency gaps by annihilations of the Weyl points, novel transmission properties and other unconventional phenomena associated with the density of states and dispersion relations close to the degeneracy points.

Received 26 July 2012; accepted 3 February 2013; published online 17 March 2013

References

1. Castro Neto, A. H., Guinea, F., Peres, N. M. R., Novoselov, K. S. & Geim, A. K. The electronic properties of graphene. *Rev. Mod. Phys.* **81,** 109–162 (2009).
2. Bonaccorso, F., Sun, Z., Hasan, T. & Ferrari, A. C. Graphene photonics and optoelectronics. *Nature Photon.* **4,** 611–622 (2010).
3. Sepkhanov, R. A., Bazaliy, Y. B. & Beenakker, C. W. J. Extremal transmission at the Dirac point of a photonic band structure. *Phys. Rev. A* **75,** 063813 (2007).
4. Zhang, X. Observing *Zitterbewegung* for photons near the Dirac point of a two-dimensional photonic crystal. *Phys. Rev. Lett.* **100,** 113903 (2008).
5. Peleg, O. *et al.* Conical diffraction and gap solitons in honeycomb photonic lattices. *Phys. Rev. Lett.* **98,** 103901 (2007).
6. Bravo-Abad, J., Joannopoulos, J. D. & Soljačić, M. Enabling single-mode behavior over large areas with photonic Dirac cones. *Proc. Natl Acad. Sci. USA* **109,** 9761–9765 (2012).
7. Rechtsman, M. C. *et al.* Strain-induced pseudomagnetic field and photonic Landau levels in dielectric structures. *Nature Photon.* **7,** 153–158 (2013).
8. Hasan, M. Z. & Kane, C. L. Colloquium: topological insulators. *Rev. Mod. Phys.* **82,** 3045–3067 (2010).
9. Haldane, F. D. M. & Raghu, S. Possible realization of directional optical waveguides in photonic crystals with broken time-reversal symmetry. *Phys. Rev. Lett.* **100,** 013904 (2008).
10. Wang, Z., Chong, Y., Joannopoulos, J. D. & Soljačić, M. Observation of unidirectional backscattering-immune topological electromagnetic states. *Nature* **461,** 772–775 (2009).
11. Khanikaev, A. B. *et al.* Photonic topological insulators. *Nature Mater.* **12,** 233–239 (2013).
12. Rechtsman, M. C. *et al.* Photonic floquet topological insulators. Preprint at http://lanl.arXiv.org/abs/1212.3146 (2012).
13. Wan, X., Turner, A. M., Vishwanath, A. & Savrasov, S. Y. Topological semimetal and fermi-arc surface states in the electronic structure of pyrochlore iridates. *Phys. Rev. B* **83,** 205101 (2011).
14. Burkov, A. A. & Balents, L. Weyl semimetal in a topological insulator multilayer. *Phys. Rev. Lett.* **107,** 127205 (2011).
15. Halász, G. B. & Balents, L. Time-reversal invariant realization of the Weyl semimetal phase. *Phys. Rev. B* **85,** 035103 (2012).
16. Xu, G., Weng, H., Wang, Z., Dai, X. & Fang, Z. Chern semimetal and the quantized anomalous Hall effect in $HgCr_2Se_4$. *Phys. Rev. Lett.* **107,** 186806 (2011).
17. Volovik, G. in *The Universe in a Helium Droplet* Ch. 8 (Clarendon, 2003).
18. Yang, K-Y., Lu, Y-M. & Ran, Y. Quantum Hall effects in a Weyl semimetal: possible application in pyrochlore iridates. *Phys. Rev. B* **84,** 075129 (2011).
19. Hosur, P., Parameswaran, S. A. & Vishwanath, A. Charge transport in Weyl semimetals. *Phys. Rev. Lett.* **108,** 046602 (2012).
20. Aji, V. Adler–Bell–Jackiw anomaly in Weyl semimetals: application to pyrochlore iridates. *Phys. Rev. B* **85,** 241101 (2012).
21. Schoen, A. *Infinite Periodic Minimal Surfaces without Self-intersections*, NASA Technical Note No. D-5541 (NASA, 1970).
22. Wohlgemuth, M., Yufa, N., Hoffman, J. & Thomas, E. L. Triply periodic bicontinuous cubic microdomain morphologies by symmetries. *Macromolecules* **34,** 6083–6089 (2001).
23. Hahn, T. *International Tables for Crystallography (Volume A): Space-group Symmetry* Part 7 (Kluwer Academic, 2002).
24. Mañes, J. L. Existence of bulk chiral fermions and crystal symmetry. *Phys. Rev. B* **85,** 155118 (2012).
25. Aroyo, M. I., Kirov, A., Capillas, C., Perez-Mato, J. M. & Wondratschek, H. Bilbao crystallographic server. II. Representations of crystallographic point groups and space groups. *Acta Crystallogr. A* **62,** 115–128 (2006).
26. Maldovan, M., Urbas, A. M., Yufa, N., Carter, W. C. & Thomas, E. L. Photonic properties of bicontinuous cubic microphases. *Phys. Rev. B* **65,** 165123 (2002).
27. Burkov, A. A., Hook, M. D. & Balents, L. Topological nodal semimetals. *Phys. Rev. B* **84,** 235126 (2011).
28. Meade, R. D., Brommer, K. D., Rappe, A. M. & Joannopoulos, J. D. Electromagnetic Bloch waves at the surface of a photonic crystal. *Phys. Rev. B* **44,** 10961–10964 (1991).
29. Bouchaud, J. P. & Zérah, P. G. Spontaneous resonances and universal behavior in ferrimagnets: effective-medium theory. *Phys. Rev. Lett.* **63,** 1000–1003 (1989).
30. Bernevig, B., Hughes, T., Raghu, S. & Arovas, D. Theory of the three-dimensional quantum Hall effect in graphite. *Phys. Rev. Lett.* **99,** 146804 (2007).
31. Raghu, S. & Haldane, F. D. M. Analogs of quantum-Hall-effect edge states in photonic crystals. *Phys. Rev. A* **78,** 033834 (2008).
32. Wang, Z., Chong, Y. D., Joannopoulos, J. D. & Soljačić, M. Reflection-free one-way edge modes in a gyromagnetic photonic crystal. *Phys. Rev. Lett.* **100,** 013905 (2008).
33. Pouya, C. & Vukusic, P. Electromagnetic characterization of millimetre-scale replicas of the gyroid photonic crystal found in the butterfly parides sesostris. *Interface Focus* **2,** 645–650 (2012).

34. Özbay, E. *et al.* Measurement of a three-dimensional photonic band gap in a crystal structure made of dielectric rods. *Phys. Rev. B* **50,** 1945–1948 (1994).
35. Saba, M. *et al.* Circular dichroism in biological photonic crystals and cubic chiral nets. *Phys. Rev. Lett.* **106,** 103902 (2011).
36. Hyde, S., Andersson, S., Ericsson, B. & Larsson, K. A cubic structure consisting of a lipid bilayer forming an infinite periodic minimum surface of the gyroid type in the glycerolmonooleat-water system. *Z. Kristallogr.* **168,** 213–219 (1984).
37. Kresge, C., Leonowicz, M., Roth, W., Vartuli, J. & Beck, J. Ordered mesoporous molecular sieves synthesized by a liquid-crystal template mechanism. *Nature* **359,** 710–712 (1992).
38. Saranathan, V. *et al.* Structure, function, and self-assembly of single network gyroid ($I4_132$) photonic crystals in butterfly wing scales. *Proc. Natl Acad. Sci. USA* **107,** 11676–11681 (2010).
39. Hur, K. *et al.* Three-dimensionally isotropic negative refractive index materials from block copolymer self-assembled chiral gyroid networks. *Angew. Chem.* **123,** 12191–12195 (2011).
40. Armatas, G. S. & Kanatzidis, M. G. Mesostructured germanium with cubic pore symmetry. *Nature* **441,** 1122–1125 (2006).
41. García-Santamara, F. *et al.* A germanium inverse woodpile structure with a large photonic band gap. *Adv. Mater.* **19,** 1567–1570 (2007).
42. Ullal, C. K. *et al.* Triply periodic bicontinuous structures through interference lithography: a level-set approach. *J. Opt. Soc. Am. A* **20,** 948–954 (2003).
43. Turner, M., Schröder-Turk, G. & Gu, M. Fabrication and characterization of three-dimensional biomimetic chiral composites. *Opt. Express* **19,** 10001–10008 (2011).
44. Yablonovitch, E., Gmitter, T. J. & Leung, K. M. Photonic band structure: the face-centered-cubic case employing nonspherical atoms. *Phys. Rev. Lett.* **67,** 2295–2298 (1991).
45. Takahashi, S. *et al.* Direct creation of three-dimensional photonic crystals by a top-down approach. *Nature Mater.* **8,** 721–725 (2009).
46. Lu, L. *et al.* Three-dimensional photonic crystals by large-area membrane stacking. *Opt. Lett.* **37,** 4726–4728 (2012).

Acknowledgements

The authors thank F. Wang, M. Maldovan, Y. Ran, Z. Wang, S. G. Johnson, A. Vishwanath and D-H. Lee for helpful discussions. This work was supported in part by the US Army Research Office through the Institute for Soldier Nanotechnologies (contract no.W911NF-07-D-0004). L.L. was supported in part by the Materials Research Science and Engineering Center of the National Science Foundation (award no. DMR-0819762). M.S. and L.L. were supported in part by the Massachusetts Institute of Technology S3TEC Energy Frontier Research Center of the US Department of Energy (grant no. DE-SC0001299). L.F. was supported by start-up funds from MIT.

Author contributions

L.L. proposed the gyroid photonic crystal system for realizing Weyl points and performed the simulations. L.F. developed a low-energy k.p model for the proposed system. All authors contributed to the design of the study, discussion of the results and writing of the manuscript.

Additional information

Supplementary information is available in the online version of the paper. Reprints and permissions information is available online at www.nature.com/reprints. Correspondence and requests for materials should be addressed to L.L.

Competing financial interests

The authors declare no competing financial interests.

nature photonics

SUPPLEMENTARY INFORMATION

DOI: 10.1038/NPHOTON.2013.42

Supplementary information for "Weyl points and line nodes in gyroid photonic crystals"

Ling Lu, Liang Fu, John Joannopoulos and Marin Soljačić

Department of Physics, Massachusetts Institute of Technology, Cambridge, Massachusetts 02139, USA

PHASE DIAGRAM

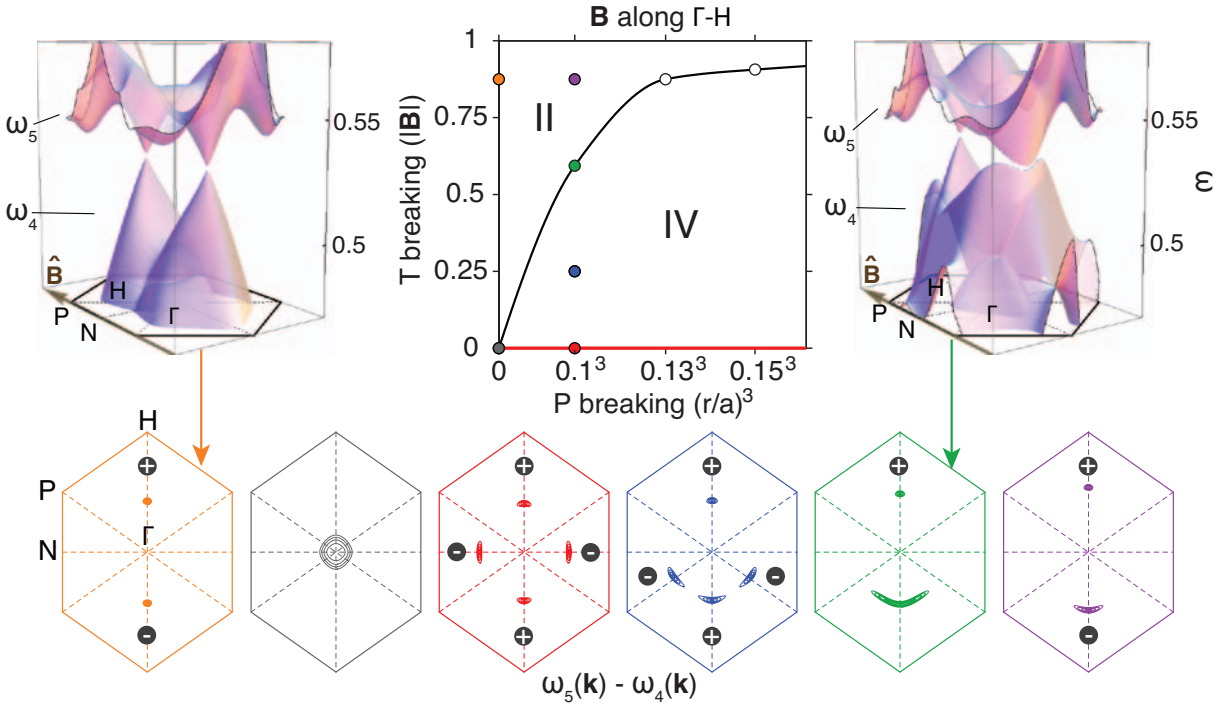

FIG. A: **Phase diagram of Weyl points when the magnetic field is applied along Γ-H.** Each phase is labeled by the number (Roman numerals) of Weyl points. The phase transition line is found by scanning the **B** field amplitude in the calculation for three different P-breaking strengths. The pure P-breaking phase (x-axis) is highlighted in red; it is realizable at the optical frequencies with essentially lossless materials. Six 2D contour plots show the locations of the Weyl points at representative positions in the phase diagram. The contour plots share the same color as the circles of their corresponding positions in the phase diagram. A few lowest-value equi-frequency contours of the frequency difference between the 4th and 5th bands are shown in each contour plot. The contour spacing is 0.002 in normalized frequency. "+" and "-" are used to label the chiralities of the Weyl points. Two surface plots show the entire band dispersions of the 3rd, 4th and 5th bands for two particular cases of the contour plots.

In Fig. A, when **B** is along Γ-H, only two phases exist: the T-breaking dominated phase (II) and the P-breaking dominated phase (IV). The annihilation and creation of Weyl points are shown by contour plots in a (101) plane through Γ, in which all the Weyl points in this article locate. The pure P-breaking phase, third (from left) contour plot in red, has four Weyl points: two with positive chiralities along Γ-H and two with negative chiralities along Γ-N. Applying magnetic field along the Γ-H direction drives the two negative-chirality Weyl points towards the positive one (blue contour plot). On the phase transition line where the three Weyl points meet (green contour plot), the dispersions of the two bands are cubic($\pm|k|^3$) along the direction which they meet, but still linear in other directions in **k** space. Increasing the magnetic field further annihilates two of the Weyl points of opposite chiralities and the system enters the T-breaking dominated phase (II) which has only two Weyl points (purple contour plot).

DOI: 10.1038/NPHOTON.2013.42

MODEL OF LOW ENERGY THEORY

In order to further elucidate the physics and to tie our work more closely to the Weyl fermions in electronics, we constructed a three-band effective Hamiltonian (H_0) with three perturbation terms (V_1, V_2 and V_3) to model the 3rd, 4th and 5th bands of the DG PhC system. This model reproduces qualitatively all the bandstructures in Fig. 2 and the phase diagram in Fig. A. In order to reproduce the phase diagram of Fig. 4, a more intricate model is required.

$$\begin{aligned} H(\mathbf{k}) &= H_0(\mathbf{k}) + V_1 + V_2(\mathbf{k}) + V_3 \\ H_0(\mathbf{k}) &= \alpha_1 |\mathbf{k}|^2 - \alpha_2 (\mathbf{k}\cdot\mathbf{L})^2 \\ V_1 &= -\gamma_1 ((\mathbf{L}\cdot\hat{\mathbf{n_p}})^2 - 1) \\ V_2(\mathbf{k}) &= \gamma_2 (\mathbf{k}\cdot\hat{\mathbf{n_0}})(\mathbf{L}\cdot\hat{\mathbf{n_0}}) \\ V_3 &= \beta (\mathbf{L}\cdot\mathbf{B}) \end{aligned} \tag{1}$$

Here $\mathbf{L} = (Lx, Ly, Lz)$ where $Lx = -i\begin{pmatrix} 0 & 0 & 0 \\ 0 & 0 & 1 \\ 0 & -1 & 0 \end{pmatrix}$, $Ly = -i\begin{pmatrix} 0 & 0 & -1 \\ 0 & 0 & 0 \\ 1 & 0 & 0 \end{pmatrix}$ and $Lz = -i\begin{pmatrix} 0 & 1 & 0 \\ -1 & 0 & 0 \\ 0 & 0 & 0 \end{pmatrix}$. $\mathbf{L}$ is the angular momentum; it is odd under T and even under P. $\hat{\mathbf{n_p}} = \frac{1}{\sqrt{2}}(1,0,1)$ is perpendicular to the Γ-N-P-H (101) plane where all the degeneracies lie in. $\hat{\mathbf{n_0}} = \frac{1}{\sqrt{2}}(-1,0,1)$ is along Γ-N. $\mathbf{B}$ is the external magnetic field. α_1, α_2, γ_1, γ_2 and β are positive real parameters that control the relative strengths of the different terms in the Hamiltonian.

The original Hamiltonian H_0[1] produces the three-fold quadratic degeneracy at zero energy, same as the PhC bandstructure at Γ in Fig. 2**a**. α_1 controls the curvature of the top band; α_2 controls the curvatures of the two degenerate bands concaving down.

Perturbation V_1 breaks neither P nor T symmetries. This perturbation lifts the three-fold degeneracy at Γ while keeping the quadratic degeneracy between the lower two bands at zero energy: this reproduces the line-node result in Fig. 2**b**.

Perturbation V_2 breaks P. V_1 and V_2 together reproduce the two pairs of Weyl points along Γ-N and Γ-H in Fig. 2**c**.

Perturbation V_3 breaks T. When this perturbation is turned on alone, a pair of Weyl points of opposite chiralities emerge along the direction of the magnetic field (**B**), which is consistent with our PhC result in Fig. 2**d**.

When all three perturbation terms are non-zero, this model reproduces the same II-IV phase diagrams in Fig. A (i.e. when **B** is along Γ-H).

ACCIDENTAL LINEAR-DEGENERACIES AND 3D DIRAC POINTS

2D or 3D linear dispersions of two bands can also exist when being accidentally degenerate among other bands at the Brillouin zone (BZ) center; but those points do not possess any topological features[2–4], so they are quite different from the work presented here.

A 3D Dirac point [5] is a linear point degeneracy between four bands; it consists of two Weyl points of opposite chiralities. The low energy theory satisfies the 4 by 4 Dirac equation which reduces to two 2 by 2 Weyl equations when the mass terms are zeros. 3D Dirac points can exist with PT symmetry. The Chern number of a 3D Dirac point is zero, so it is not robust in the momentum space.

[1] Chong, Y. D., Wen, X.-G. & Soljačić, M. Effective theory of quadratic degeneracies. *Phys. Rev. B* **77**, 235125 (2008).

[2] Huang, X., Lai, Y., Hang, Z. H., Zheng, H. & Chan, C. T. Dirac cones induced by accidental degeneracy in photonic crystals and zero-refractive-index materials. *Nature Mater.* **10**, 582–586 (2011).

[3] Sakoda, K. Dirac cone in two- and three-dimensional metamaterials. *Opt. Express* **20**, 3898–3917 (2012).

[4] Huang, X., Liu, F. & Chan, C. T. Three dimensional Dirac point at k=0 in photonic and phononic systems. *ArXiv e-prints* (2012). 1205.0886.

[5] Young, S. M. *et al.* Dirac semimetal in three dimensions. *Phys. Rev. Lett.* **108**, 140405 (2012).